ISPRS Journal of Photogrammetry and Remote Sensing 128 (2017) 338–353

Contents lists available at ScienceDirect

ISPRS Journal of Photogrammetry and Remote Sensing

journal homepage: www.elsevier.com/locate/isprsjprs

Effects of urban tree canopy loss on land surface temperature magnitude and timing

Arthur Elmes [a,*], John Rogan [a], Christopher Williams [a], Samuel Ratick [a], David Nowak [b], Deborah Martin [a]

[a] Graduate School of Geography, Clark University, 950 Main Street, Worcester, MA 01610, USA
[b] USDA Forest Service, Northern Research Station, 5 Moon Library, SUNY-ESF, Syracuse, NY 13215, USA

ARTICLE INFO

Article history:
Received 22 September 2016
Received in revised form 14 April 2017
Accepted 14 April 2017

Keywords:
Urban heat island
Seasonal trends analysis
Urban forestry
Image segmentation
Land surface temperature
Urban tree canopy mapping

ABSTRACT

Urban Tree Canopy (UTC) plays an important role in moderating the Surface Urban Heat Island (SUHI) effect, which poses threats to human health due to substantially increased temperatures relative to rural areas. UTC coverage is associated with reduced urban temperatures, and therefore benefits both human health and reducing energy use in cities. Measurement of this relationship relies on accurate, fine spatial resolution UTC mapping, and on time series analysis of Land Surface Temperatures (LST). The City of Worcester, Massachusetts underwent extensive UTC loss and gain during the relatively brief period from 2008 to 2015, providing a natural experiment to measure the UTC/LST relationship. This paper consists of two elements to this end. First, it presents methods to map UTC in urban and suburban locations at fine spatial resolution (~0.5 m) using image segmentation of a fused Lidar/WorldView-2 dataset, in order to show UTC change over time. Second, the areas of UTC change are used to explore changes in LST magnitude and seasonal variability using a time series of all available Landsat data for the study area over the eight-year period from 2007 to 2015. Fractional UTC change per unit area was determined using fine resolution UTC maps for 2008, 2010, and 2015, covering the period of large-scale tree loss and subsequent planting. LST changes were measured across a series of net UTC change bins, providing a relationship between UTC net change and LST trend. LST was analyzed for both monotonic trends over time and changes to seasonal magnitude and timing, using Theil-Sen slopes and Seasonal Trend Analysis (STA), respectively. The largest magnitudes of UTC loss occurred in residential neighborhoods, causing increased exposure of impervious (road) and pervious (grass) surfaces. Net UTC loss showed higher monotonic increases in LST than persistence and gain areas. STA indicated that net UTC loss was associated greater difference between 2008 and 2015 seasonal temperature curves than persistence areas, and also larger peak LST values, with peak increases ranging from 1 to 6 °C. Timing of summer warm period was extended in UTC loss areas by up to 15 days. UTC gain provided moderate LST mitigation, with lower monotonic trends, lower peak temperatures, and smaller seasonal curve changes than both persistence and loss locations. This study shows that urban trees mitigate the magnitude and timing of the surface urban heat island effect, even in suburban areas with less proportional impervious coverage than the dense urban areas traditionally associated with SUHI. Trees can therefore be seen as an effective means of offsetting the energy-intensive urban heat island effect.

1. Introduction

Urban areas experience elevated temperatures relative to surrounding non-urbanized areas due to alteration of land-cover, in what is known as the Urban Heat Island (UHI) (Oke, 1982; Voogt and Oke, 2003; Weng, 2001). Previous research has convincingly documented that increased temperatures are a function of proportional coverage and spatial configuration of impervious surfaces within dense urban sites (Maimaitiyiming et al., 2014; Solecki et al., 2005; Weng, 2009; Weng et al., 2007). However, less attention has been given to temperature elevations in low density residential areas, which have a comparatively greater proportional cover of grass and other non-tree vegetation. Quantification of the temperature effects of land cover in these areas is critically important due to the large amount of energy used in home cooling (Akbari, 2002; Pandit and Laband, 2010). This paper draws on a

* Corresponding author at: 950 Main Street, Worcester, MA 01610, USA.
E-mail address: aelmes@clarku.edu (A. Elmes).

http://dx.doi.org/10.1016/j.isprsjprs.2017.04.011

dense time series of eight years of thermal data to investigate local alterations to the UHI caused by Urban Tree Canopy (UTC) change.

UTC coverage is closely tied to LST, because trees provide shading, increased evaporative cooling, and lower thermal absorption and retention (McPherson and Simpson, 2003; Nowak and Dwyer, 2007; Solecki et al., 2005). Absence of UTC coverage in urban areas causes the increase in LST, causing the Surface Urban Heat Island (SUHI) effect, which is a component of the overall UHI (Voogt and Oke, 2003). Therefore, one of the major ecosystem services provided by urban forests is the reduction of the SUHI effect by reducing LST, which translates to reduced cooling energy demands and reduced risks to increased human health and comfort (Cui and De Foy, 2012; Hamada and Ohta, 2010; Nowak and Dwyer, 2007). In Worcester, Massachusetts, several state and federal government reports provide qualitative evidence suggesting that residents in the city have experienced marked thermal discomfort and increased energy bills due to tree removal, particularly during summer months of June through September, when air conditioning creates a large demand for electrical energy (Morzuch, 2013; Palmer et al., 2014). The case of Worcester is relevant to understanding SUHI/LST dynamics because the majority of tree removal and planting in the city since 2008 has occurred in lower density private residential areas, rather than in more densely urbanized areas (Hostetler et al., 2013), which contain a much larger total population of residents than dense urban areas typically investigated for heat island effects. Therefore, this study investigates the cooling benefits of trees in areas with mixed vegetation and impervious cover composition, using four scales of analysis: city, neighborhood, street, and parcel. This approach allows the exploration of the scalar nature of the UTC/LST relationship, showing the heterogeneity of UTC loss and corresponding LST change, and can therefore illustrate the importance of neighborhood-wide urban forestry efforts.

The research described in this paper analyzes the impact of Urban Tree Canopy (UTC) change on LST magnitude and seasonal timing, using a case study in Worcester, Massachusetts, USA. This study area was selected due to an extremely large amount of tree canopy change over the brief period from 2008 to 2015. This change occurred predominantly in low density residential areas (Hostetler et al., 2013), which comprise a complex patchwork of impervious surfaces, grass/lawn area, small and large trees, and exposed soils (Rogan et al., 2013). Therefore, the canopy change has exposed a mixture of impervious and pervious surfaces. Hypothetically, LST increases in these low density residential locations due to canopy loss potentially present a weaker signal compared to dense and highly built urban locations, allowing for a more nuanced quantification of this relationship, while also providing a test of the capability of remotely measured LST.

The goals of this study were to: (1) create an up-to-date, high spatial resolution UTC map of Worcester to monitor the dynamic UTC conditions; and (2) quantify the magnitude and seasonality of LST change between 2007 and 2015 within locations of UTC gain, loss, and persistence. The relationship between UTC reduction and LST increase is explored at the city, neighborhood, street, and individual property-parcel scales. Remote sensing provides an ideal basis for this analysis due to the utility of high-resolution imagery for effectively mapping fine-scale UTC changes, and the ability to investigate nuanced temperature trends and cycles using the large collection of thermal images available over the study period.

2. Study area

Worcester is located in central Massachusetts, USA (Fig. 1). With a population of 183,000 and a population density of 1808 persons/km^2, it is the second largest city in New England after Boston. Worcester covers approximately 100 km^2, and has a heterogeneous land-use pattern and composition typical of medium-sized cities in temperate climates, comprising a mixture of high- and low-density residential development, woodland areas, and impervious surfaces (Rogan et al., 2010), typical of many mid-latitude temperate urban centers. Worcester has a humid continental climate, with an average daily high of 26 °C in July and 0 °C in January. Average annual precipitation is 1220 mm, as well as 163 cm of snow per season (www.nws.noaa.gov 2015). Elevation ranges from 110 to 320 m above sea level. Worcester's urban forest consists of a mixture of hardwood and conifer species, with 51% hardwood, 11% conifer, and 38% mixed (Hall et al., 2002; Rogan et al., 2010). As of 2008, Worcester had 17,113 street trees, providing roughly $2.4 million dollars of gross ecosystem service benefits, or $980,000 of net benefits after subtracting maintenance and management (Freilicher et al., 2008). In addition to these street trees, Worcester contains a large (as-yet uncounted) number of trees on public and private property, which constitute the bulk of the UTC for the study area.

Worcester's urban forest has been greatly influenced by large climatological, biological, and anthropogenic disturbance events, culminating in the recent Asian Longhorned Beetle infestation. These disturbance events have prompted several extensive planting efforts to rebuild the urban forest, resulting in a highly dynamic urban forest (Herwitz, 2001). During the 20th century, these efforts relied heavily on just a few species of trees, especially the *Acer* (maple) genus, which was favored for its urban adaptability, and which ultimately came to constitute 80% of street trees as of 2008 (Freilicher, 2011; Freilicher et al., 2008). This near-monoculture approach has made the city vulnerable to outbreaks of invasive species, which precipitated the city's most recent UTC disturbance, caused by the invasive insect, the Asian Longhorned Beetle (*Anoplophora glabripennis*, ALB) infestation. This infestation was first identified in 2008 (Dodds and Orwig, 2011), and continues to date (2017), presenting an ongoing urban forest management problem and a large quantity of UTC change in a short time period. To exterminate ALB, roughly 30,000 mature trees have been removed, the bulk of which were removed from the Burncoat and Greendale residential neighborhoods in the north of Worcester (Santos and Cole, 2012; WTI, 2015). Approximately 65 ha of UTC was removed by 2010, a 21% decrease in UTC relative to 2008. Previous research mapped UTC at 1 m spatial resolution for the years 2008 and 2010, providing a basis for comparison, as well as further contextual knowledge of the study area (Hostetler et al., 2013). This dramatic UTC changeover provides an ideal natural experiment to investigate the temperature mitigation effect of urban tree cover.

3. Data

To determine the effect of UTC change on LST, two datasets were assembled and analyzed: the first involves high spatial resolution mapping of UTC and therefore UTC change, and the second involves LST. High resolution mapping provided the context for LST trend analysis; the data and methods for UTC mapping are described in Sections 3.1 and 4.1 below. LST time series analysis is described in Sections 3.2 and 4.2.

3.1. UTC mapping: fine spatial resolution imagery and Lidar data

The first stage of the analysis involves UTC change detection between 2008, 2010, and 2015, corresponding to the periods: (1) directly before tree removal; (2) directly after tree removal; and (3) after tree planting. Two existing 1 m UTC maps of Worcester

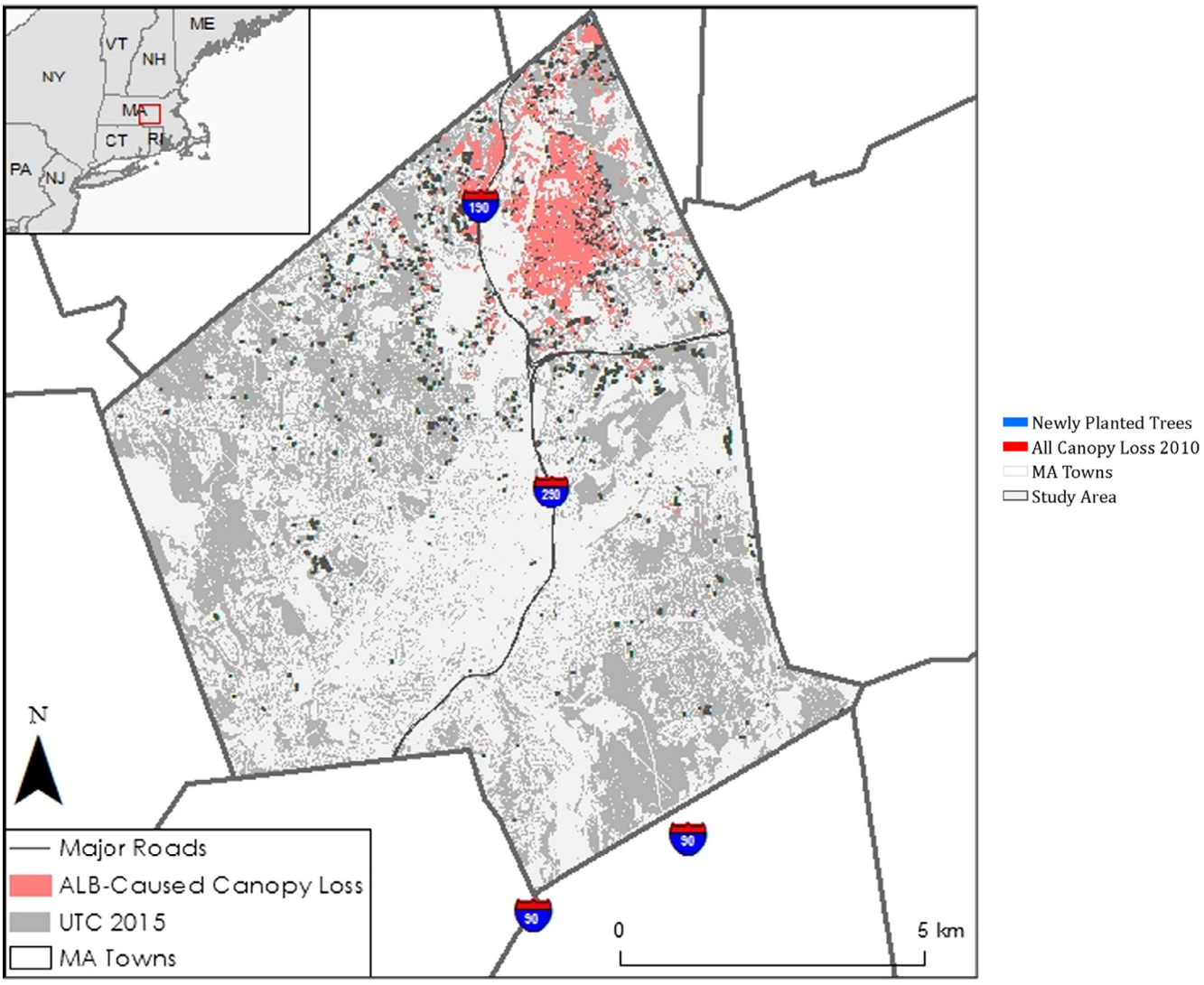

Fig. 1. Study area map, showing 2008–2010 Urban Tree Canopy (UTC) loss areas, created by Hostetler et al. (2013).

Table 1
Summary of datasets used for UTC mapping and LST time series analysis.

Dataset	Date	Resolution	Purpose
Landsat TM, ETM+, OLI/TIRS	1/1/2007 – 12/31/2015	Multispectral: 30 m; Thermal: 120 m (TM), 60 m (ETM+), 100 m (TIRS)	Land Surface Temperature measurement, facilitating temperature trend analysis
WorldView-2 multispectral/panchromatic	5/7/2015	2 m multispectral, 0.5 m pan	Urban Tree Canopy mapping. The spectral data for the pixel-based classification, which was enhanced by the segmentation
USGS/FEMA Lidar	1/2013 – 5/2014	0.7 m minimum ground return spacing. Pulse rate: 272 kHz, Scan rate: 42.3 Hz, Side lap: 25%	Urban Tree Canopy Mapping. Eight rasters were created from the Lidar data: canopy coverage %, canopy density, maximum, minimum, and mean canopy height, skewness, kurtosis, standard deviation
Weather Station Temperature and Water Vapor	1/1/2007 – 12/31/2015	Daily values from 4 permanent stations in study area	Used in LST derivation, accounting for atmospheric water vapor contribution to raw thermal values

were available for 2008 and 2010 from the University of Vermont Spatial Analysis Lab (https://www.uvm.edu/rsenr/sal/). The UTC maps were created using 1 m National Agriculture Imagery Program (NAIP) true-color aerial imagery and object-based imagery analysis within the eCognition software package (see Table 1) (Hostetler et al., 2013). The 2015 UTC map was created using a combination of airborne Lidar and WorldView-2 multispectral satellite imagery (DigitalGlobe, 2015). The Lidar data were captured between November 16, 2013 and April 20, 2014 by Woolpert, Inc. as part of a joint effort between the Federal Emergency Management Agency (FEMA) and the United States Geological Survey (USGS). The data have a nominal post-spacing of 0.7 m, a 4 return (echo) capability, and vertical RMS error of 0.052 m. Because of its ability to penetrate tree and shrub canopies, Lidar contributes vegetation structural information, which is particularly valuable for differentiating tree canopy from spectrally similar grass and

shrubs (Dalponte et al., 2008). The Lidar data complemented the 2.5 m WorldView-2 multispectral satellite imagery captured on 05/2015, which were pan-sharpened using the included panchromatic band to enhance spatial resolution to 0.5 m. WorldView-2 data comprise of eight spectral bands ranging from 400 to 1040 nm, which facilitates reliable vegetation mapping over a background of impervious and other exposed urban surfaces.

The UTC map validation data consisted of 500 points placed randomly throughout two strata: UTC and non-UTC, based on a preliminary classification. The true category of each site was defined using Google Earth™, whose most recent high-resolution imagery of the study area was collected on May 6 of 2015, very close to the 0.5 m WorldView-2 imagery used in this study. The Google Earth imagery for this time and location is of higher spatial resolution than the WorldView-2 data used for UTC mapping. Extensive fieldwork also provided the authors with familiarity with the study area.

3.2. Landsat-derived land surface temperature time series

The second stage of the analysis relied on a time series of eight years of thermal data from Landsat TM, ETM+, and OLI/TIRS. The 2007 to 2015 temporal window encompasses the period of UTC removal and subsequent tree planting, with a one-year pre-removal baseline at the beginning of the series. The analysis used all available images from path/rows 12/31, 13/30, and 13/31 between 1/1/2007 and 12/31/2015, regardless of cloud cover. This series comprised 891 distinct dates, with 1319 distinct images, owing to the two scenes from path 13 rows 30 and 31, which are acquired on the same day. Overlap between these two rows was eliminated by removing overlap pixels from path 13, row 31.

To maximize data completeness, a pixel stack approach selected every cloud-free pixel in the time series, regardless of the overall cloud cover percentage of a given image. This approach relied on the USGS-generated cloud, snow, and shadow mask bundled with each image delivered via the EarthExplorer platform for Landsat Surface Reflectance products, created using the CFMask algorithm (Zhu and Woodcock, 2012). LST derivation relied on the thermal data (band 6, 10.4–12.5 μm, for TM and ETM+, band 10, 10.6–11.19 μm, for TIRS) were acquired from the Landsat Level 1 product, while the spectral and cloud mask bands were acquired from the Landsat Surface Reflectance High Level product. These surface reflectance products are generated server-side on www.earthexplorer.usgs.gov using Landsat Ecosystem Disturbance Adaptive Processing System (LEDAPS) for Landsat TM and ETM+, and an equivalent process for Landsat OLI/TIRS (Schmidt et al., 2013). A mean LST image was calculated for each month in the time period, yielding 96 total LST images for time series analysis. Cloud-masked pixels were excluded from the averaging process, which helped alleviate data gaps in the time series.

4. Methods

This project relied on two stages of analysis. First, UTC was mapped in fine spatial detail for the most recent date possible, which complemented two existing UTC maps of similar spatial characteristics from 2008 and 2010. These three UTC maps provided the basis for UTC change detection, which was aggregated to the coarser Landsat resolution, producing a 30 m grid of net UTC change. The second stage involved a time series analysis of all available Landsat thermal imagery, from which LST was derived. The net UTC change grid produced in the first stage was used to analyze LST pixel stacks separately, depending on their associated level of net UTC change. Ultimately, this allows for comparison of LST trends in UTC loss, persistence, and gain locations.

4.1. UTC mapping and change analysis

Fine spatial resolution (i.e., ~1 m) UTC mapping is critical for urban forest inventory and change analysis (Moskal et al., 2011; Nowak and Greenfield, 2012; Pu and Landry, 2012). However, the character of urban forests is highly heterogeneous, ranging from intact stands of tens or hundreds of trees to lines of street-adjacent trees to individual trees in residential and institutional lawn areas (McPherson et al., 1994). This fine grained complexity renders traditional pixel-based classification of multispectral imagery difficult or impossible, and so alternative approaches such as image segmentation of high spatial resolution imagery are warranted (Ke and Quackenbush, 2007; Kim et al., 2011; O'Neil-Dunne et al., 2014). The purpose of image segmentation is to improve categorical map accuracy by including additional spatial information such as contiguity, texture, and shape not available in traditional pixel-based classifiers (Blaschke, 2010; Dey et al., 2010). This approach is particularly helpful for H-resolution scenes (sensu Strahler et al., 1986).

Aerial Lidar and WorldView-2 imagery provided the basis for the 2015 UTC map. Using the Lidar pulse return (echo) cardinality, eight canopy-specific rasters were derived from the original Lidar point cloud: mean, maximum, and minimum height; skewness; kurtosis; standard deviation; canopy coverage; and canopy density. These metrics were selected because each contains slightly different information regarding tree canopy, while it was unknown which if any would contain all necessary information for segmentation. The canopy metrics were rasterized using the same pixel grid as the WorldView-2 data, such that all sixteen image grids could be overlaid precisely, facilitating the segmentation procedure.

A variety of image segmentation methods exist; this study relied on the segmentation algorithm in the TerrSet GIS software package (Eastman, 2015), a potentially more cost-effective approach for land managers. This tool operates by subdividing input raster bands into homogenous regions that represent scene objects. This tool consists of three steps: (1) creation of a local variance image based on all input rasters using a moving window; (2) delineation of segments based on a watershed process that 'floods' pixels with low local variance; and (3) merging of adjacent segments with acceptable similarity of segment means and variances. The user defines four parameters that dictate segment size, and because the size of target objects relative to image pixel size could potentially be different for any given scene, the segmentation is highly sensitive to these parameters, and no single parameterization is equally optimal for all projects or user needs (Brenner et al., 2012).

The TerrSet implementation of segmentation-based classification also requires a pixel-based classification, in order to assign classes to the image segments. A random forests (RF) classification (Breiman, 2001). of WorldView-2 imagery carried out in the R scripting language (R Core Team, 2013) provided this preliminary map with the following categories: tree, grass, building, paved surface, bare soil, and water. These categories were ultimately reduced to UTC and non-UTC in the final map, yielding a binary map of UTC presence at 0.5 m spatial resolution. The original six classes were condensed into two classes because the only class of interest was tree, and validation was therefore concerned only with identifying this class versus any other. An example of the UTC mapping process, with a Worldview-2 composite in the background, Lidar-derived average canopy height shown in greyscale, and image segments shown in yellow is shown in Fig. 2.

Optimal values for the segmentation parameters were determined by sequentially modulating each in turn, generating a segmented UTC map, and recording the accuracy using on the Kappa Index of Agreement (KIA) with reference to previously created val-

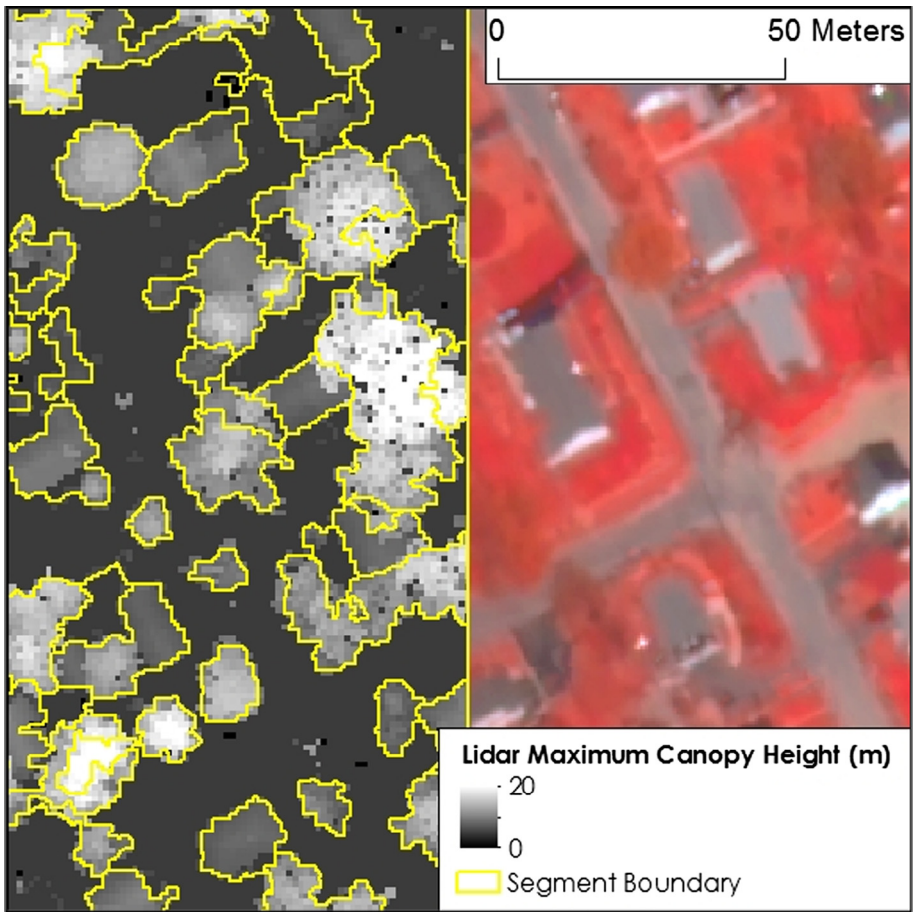

Fig. 2. Urban Tree Canopy (UTC) delineation image, showing two example input layers: Lidar-derived average canopy height and Worldview-2 imagery (CIR composite shown).

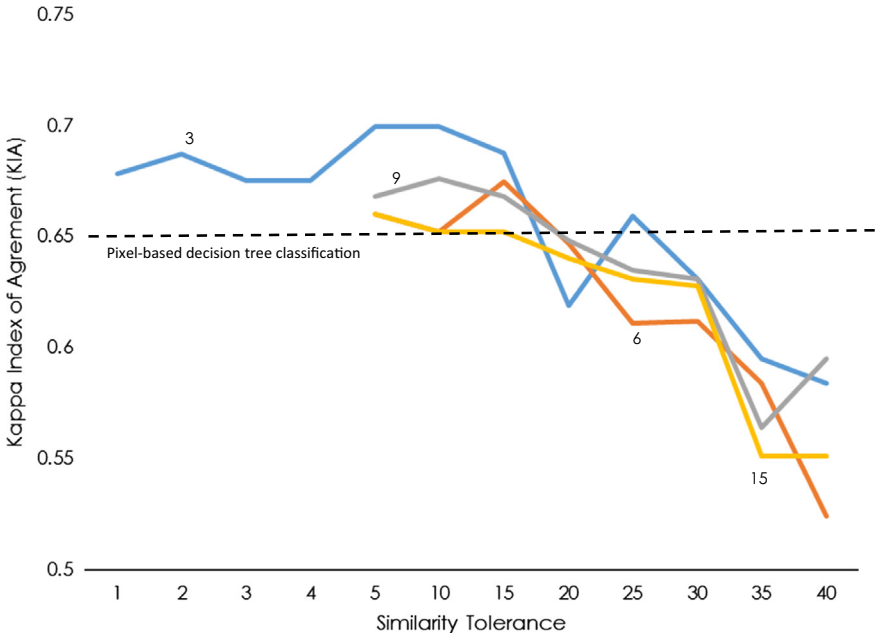

Fig. 3. Effect of segmentation parameter modulation on accuracy rates (Kappa Index of Agreement, KIA). The lines indicate the various window widths used: 3, 6, 9, or 15. The x-axis shows the similarity tolerance iterations. The horizontal dotted line indicates the accuracy of the pixel-based Random Forests map.

idation sites, as indicated graphically in Fig. 3. This figure shows KIA as a function of similarity tolerance, with each data series representing a window size. Modulation of mean and variance weights is shown graphically in Fig. 4, which shows KIA as a function of mean weight, with data series representing similarity tolerance/window size pairs. Since mean and variance weights sum to

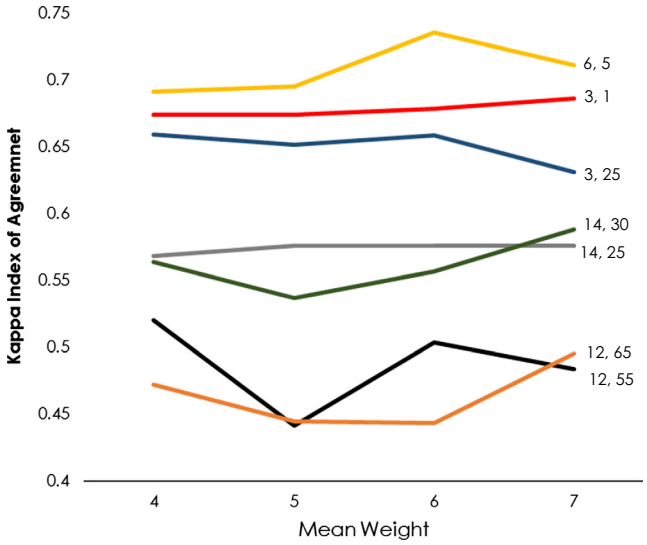

Fig. 4. Another view of the effect of segmentation parameter modulation on accuracy rates (Kappa Index of Agreement, KIA). The lines indicate the various window widths used, while the x-axis shows the similarity tolerance iterations.

1, variance weight can be inferred from this graph. The optimal segmentation parameters were used to segment and classify the study area, yielding a binary UTC/non-UTC map for 2015. This map was converted from raster to vector format in order to compliment the 2008 and 2010 binary UTC maps created previously, which had positional accuracy of ±2 m.

In order to analyze the 30 m spatial resolution Landsat-derived LST time series using the 0.5 m resolution UTC maps, fractional UTC images were created on the Landsat 30 m grid. For these new fractional UTC maps, each pixel's value represented the proportional areal coverage of UTC within that pixel. UTC increases, decreases, and persistence were then calculated by subtraction of the earlier time period UTC value from the later, yielding net change; this was conducted for 2008–2010 as well as 2008–2015, yielding two net UTC change rasters at 30 m spatial resolution. These rasters were then binned in increments of 10% fractional UTC value in order to approximate a continuous variable for UTC change. Therefore, -100% indicates pure UTC loss, while 100% represents pure UTC gain. In order to accommodate map error, UTC persistence included values from -5% to 5%, and therefore the bin boundaries end in 5 (5–15%, 15–25%, 25–35%, etc.). These bins of net UTC change were used as inputs for the subsequent LST time series analysis, allowing the testing of the hypothesis that UTC loss increases LST, while UTC gain mitigates LST.

4.2. LST derivation and time series analysis

4.2.1. LST derivation

Time series analysis was performed on all available Landsat images for the study area and time period, as defined above. Two primary obstacles complicate LST retrieval from satellite sensors: atmospheric effects and Land Surface Emissivity (LSE), both of which are accounted for using the methods described below. LST is typically derived using single- or dual-channel methods, depending on sensor spectral resolution (Li et al., 2013; Wan and Dozier, 1996). Landsat TM and ETM+ each have a single thermal channel (10.4–12.5 μm) with spatial resolution of 120 m and 60 m for Landsat 5 and 7, respectively, while Landsat TIRS has two channels at 100 m (10.6–11.19 μm; 11.5–12.51 μm). These data have high spatial resolution relative to other widely available TIR sensors (e.g. MODIS, AVHRR 1 km), and have better temporal and spatial availability than ASTER TIR data. A stray light error has yielded the longer waveband unusable, and therefore single-channel (i.e. mono-window) approaches have been recommended by NASA (http://landsat.usgs.gov/calibration_notices.php).

Single-channel algorithms traditionally require *in situ* radiosoundings and a radiative transfer model such as MODTRAN (Berk et al., 2003) to account for atmospheric absorption and emittance; however, the methods used for this analysis obviate this requirement by requiring only *in situ* water vapor content, and therefore allow for operational use of the single Landsat TIR band. This approach, referred to as $SC^{JM\&S}$, was developed by Jiménez-Muñoz and Sobrino (2003) and was updated for Landsat ETM+ and TIRS by Jiménez-Muñoz et al. (2009, 2014), respectively. It has been shown to produce acceptably low errors that are similar to more data- and time-intensive methods that rely on a full *in situ* radiosounding, with the $SC^{JM\&S}$ methods producing RMSD = 0.9 K and the full radiosounding showing an only slightly better RMSD = 0.6 K (Sobrino et al., 2004). Full *in situ* radiosounding is not feasible for long, dense time series. For regions of moderate atmospheric water content (water vapor between 0.5 and 2 $g * cm^{-2}$), the $SC^{JM\&S}$ approach has expected errors between 1 and 2 K (Cristóbal et al., 2009; Jiménez-Muñoz et al., 2014, 2009).

$SC^{JM\&S}$ first calculates at-sensor brightness temperature based on coefficients provided in the image metadata, and then corrects for atmospheric optical depth to derive LST in kelvin. LSE is estimated using proportional coverage of vegetation, as described below (Sobrino et al., 2008). Atmospheric correction uses a series of so-called atmospheric functions, empirically derived for global moderate moisture conditions, and localized with *in situ* water vapor content from local weather stations. The atmospheric functions account for atmospheric transmissivity, upwelling, and downwelling irradiance, and were derived by simulation of MODTRAN code (Jiménez-Muñoz et al., 2009; Jiménez-Muñoz and Sobrino, 2003). The calculation of these atmospheric functions is shown in Eq. (1), in which ψ is the atmospheric function and ω is atmospheric water vapor content.

$$\begin{bmatrix}\psi_1\\ \psi_2\\ \psi_3\end{bmatrix} = \begin{bmatrix}0.04019 & 0.02916 & 1.01523\\ -0.38333 & -1.50294 & 0.20324\\ 0.00918 & 1.36072 & -0.27514\end{bmatrix}\begin{bmatrix}\omega^2\\ \omega\\ 1\end{bmatrix}\begin{bmatrix}\omega^2\\ \omega\\ 1\end{bmatrix}\begin{bmatrix}\omega^2\\ \omega\\ 1\end{bmatrix} \quad (1)$$

The two parameters delta (δ) and gamma (γ) are obtained from a linear approximation of Planck's law (Jiménez-Muñoz and Sobrino, 2003), determined from the at-sensor radiance (T_{sen}), at-sensor brightness temperature (L_{sen}), and a sensor-specific conversion constant ($b\gamma$), as shown in Eqs. (2) and (3).

$$\delta \approx T_{sen} - \frac{T_{sen}^2}{b_\gamma} \quad (2)$$

$$\gamma \approx \frac{T_{sen}^2}{b_\gamma L_{sen}} \quad (3)$$

The final $SC^{JM\&S}$ LST calculation combines these coefficients, along with LSE, as described below and shown in Eq. (4), where ε is land surface emissivity and T_s is LST.

$$T_s = \gamma\left[\frac{1}{\epsilon}(\psi_1 L_{sen} + \psi_2) + \psi_3\right] + \delta \quad (4)$$

LSE relates radiant temperature, observed by a satellite, to the kinetic temperature, i.e., LST (Li and Becker, 1993; Ottle and Stoll, 1993). Accounting for LSE is essential, since emissivity errors of 1% can cause LST retrieval errors ranging from 0.3 K to 0.7 K, depending on atmospheric moisture and temperature conditions (Dash et al., 2002). While LSE correction is challenging given the

highly variable emissivity associated with heterogeneous urban land-covers (Mitraka et al., 2012), operational methods for emissivity estimation have been successfully demonstrated. This study relies on one such method, using proportional vegetation coverage to estimate LSE. This method was first described by Van de Griend and Owe (1993) and further described by Valor and Caselles (1996) and Sobrino and Raissouni (2000). Using these methods, NDVI is used to estimate vegetation proportional coverage, which in turn is used to calculate the emissivity raster for each corresponding thermal image. This allows accurate LST estimation for each date. The method models LSE as a continuous function of vegetation and soil fractional coverage per pixel, with NDVI used as an operational metric of vegetation proportional coverage. For pure vegetation (proportion of vegetation > 0.5) or pure soil (proportion of vegetation < 0.2) pixels, a pre-determined LSE value is applied, as the dominant land cover class overwhelms the other's emissivity contribution. For mixed pixels (0.2 < proportion vegetation < 0.5), LSE is continuously modeled as a function of vegetation proportion, using Eq. (5),

$$\varepsilon_m = \varepsilon_s(1 - P_v) + \varepsilon_v P_v \quad (5)$$

where ε_m is mixed pixel emissivity, ε_s is soil emissivity of 0.97, ε_v is vegetation emissivity of 0.99, and P_v is vegetation fractional coverage. P_v was modeled with Eq. (6), following Sobrino and Raissouni (2000).

$$Pv = \left(\frac{NDVI - NDVI_{min}}{NDVI_{max} - NDVI_{min}}\right)^2 \quad (6)$$

Given the large number of distinct soils, a mean soil emissivity value of 0.97 was taken from 49 soil classes from the ASTER spectral library: http://speclib.jpl.nasa.gov/ (Sobrino et al., 2008). With broad thermal bands, soil emissivity variations are low, so the use of a mean soil emissivity value is operationally appropriate; this method has been shown to produce good agreement between *in situ* sensors and remotely sensed LST, with RMSE < 0.01 (Sobrino et al., 2008). Overall, these methods are operational because of their use of widely available *in situ* data rather than radiosounding data taken at the time of image acquisition, which facilitates the use of the extensive Landsat archive.

4.2.2. LST time series analysis

The effect of UTC change on LST was investigated using three types of trend analysis: OLS regression between UTC and summer-only LST; monotonic trend analysis of all LST dates; and Seasonal Trend Analysis (STA) (Eastman et al., 2009) of all LST dates. Monotonic trend analysis relied on the Theil-Sen median slope operator (TS), which is capable of determining the trend slope of noisy data, providing a robust trend measurement (Huth and Pokorná, 2004). STA is a procedure based on harmonic analysis of each year in a time series, which extracts a set of shape parameters for the seasonal curves. STA begins by performing a harmonic regression using each image, and then uses Kendall analysis of the amplitude and phases produced by the regression (Eastman et al., 2009). Using this analysis, it is possible to determine the magnitude (i.e., amplitude) and timing (i.e., phase) of LST cycles over the course of each year.

For the first and most basic form of trend analysis, summer LST was regressed against UTC for three UTC map dates: 2008, 2010, and 2015. Summer LST (June–August) was treated as the dependent variable, with UTC the independent. Only the summer imagery was used for this portion of the analysis because the potential cooling effect of UTC is greatest at maximum greenness, and because the existing UTC maps from 2008 and 2010, as well as the new UTC map for 2015 were all generated using leaf-on imagery, summer LST data were used for each of the three regressions. To ensure maximum data coverage and lack of cloud gaps, temporally averaged LST rasters were created for each summer period, corresponding to the period bounded by June 21 to September 22. Fractional UTC for each time period, which used the same 30 m grid as Landsat, was then regressed against these summer mean LST images.

Monotonic trend metrics provide robust estimates of increase or decrease over potentially noisy remotely sensed time series. The TS operator is a non-linear trend metric, which indicates the

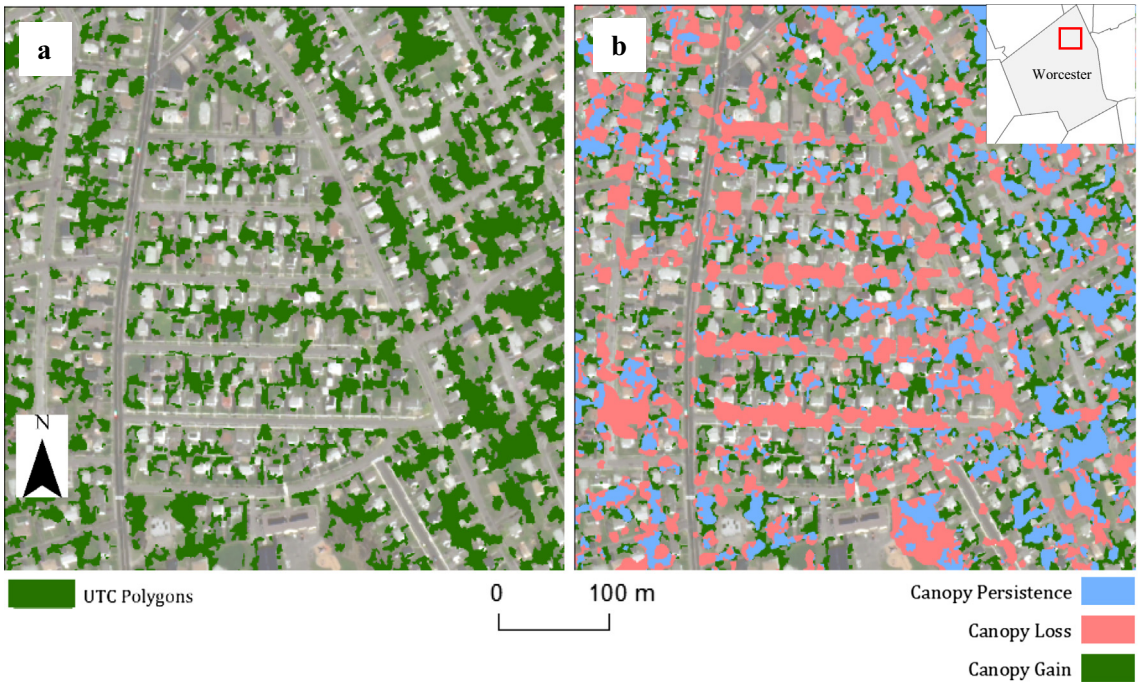

Fig. 5. Final Urban Tree Canopy (UTC) map for 2015 (a), and 2008–2015 UTC change (b).

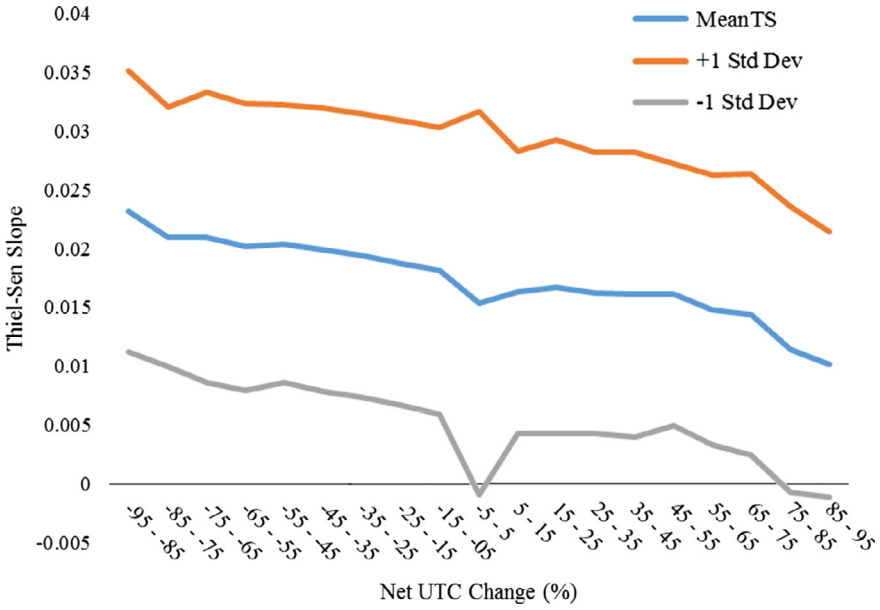

Fig. 6. Thiel-Sen median trend slope for the range of Urban Tree Canopy (UTC) bins.

median slope angle of all pairs of observations, providing a robust measure of trend (Eastman et al., 2009). A contextual Mann-Kendall significance method facilitates spatially relevant determination of monotonic trend significance (Neeti et al., 2011). Contextual Mann-Kendall significance was used to remove areas with statistically non-significant change, using a p-value threshold of 0.1. The monotonicity metric is particularly important for defining the baseline trend, a longer-term, large area temperature increase across the entire study area, not caused by UTC change.

STA summarizes changes to seasonal temperature magnitude and timing by aggregating the first and last two years of a time series, and displaying them graphically (e.g., Fig. 7). Phase (timing) changes were quantified using a warm-up and cool-down thresholds of percent of maximum, which provides the day of attainment of a given percent of maximum temperature, either during the warming or cooling phase of the season. By taking the difference in decimal days for a given warm-up/cool-down threshold, it is possible to measure the extension of the warm season experienced by the end of the time series, relative to the beginning. In order to compare the gain and loss conditions to persistence, the extension of persistence was subtracted from that of gain and loss, respectively.

Monotonicity and STA analyses were accomplished within the Earth Trends Modeler in the TerrSet GIS software package (Eastman, 2015), using the net UTC change bins to define the sample pixels. To gain a holistic perspective on the study area UTC change patterns, LST seasonality changes were explored at three scales of analysis: the entire study area of Worcester (100 km^2), the worst-hit neighborhoods of Burncoat and Greendale (~10 km^2), the individual street (~1 km^2), and individual property-parcel (~100 to 500 m^2). UTC change was analyzed at all three scales, providing information on individual- through community-level temperature change. Three metrics were used to determine changes between the seasonal curves for the beginning of the series versus the end of the series: difference in peak temperature, date of attainment of a given percent of warm-up/cool-down, and the difference between the area under the curve (AUC) for the two curves. For the latter metric, the area under the curve (AUC) was calculated for all summer dates of each seasonal curve pair, for each UTC bin, providing units of °C ∗ weeks

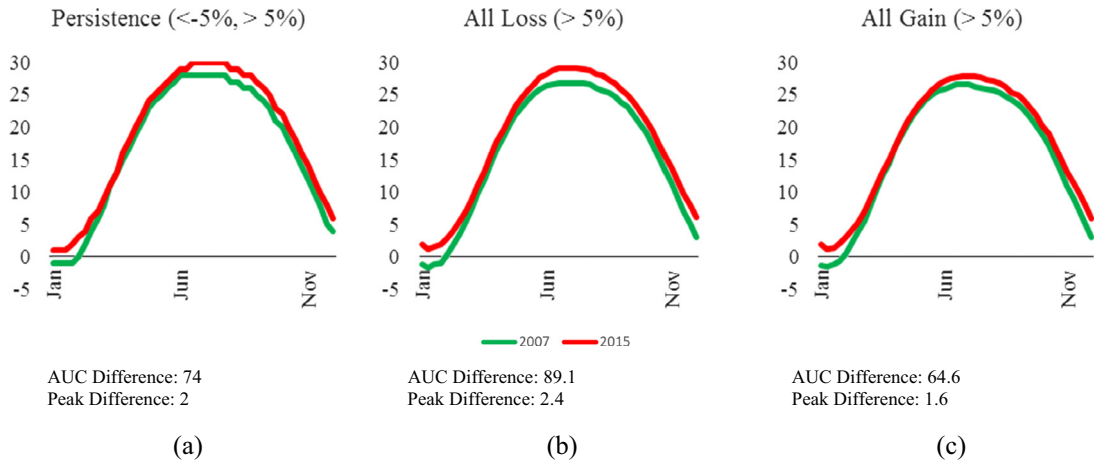

Fig. 7. Seasonal Trend Analysis (STA) curves for persistence, loss, and gain pixels. Panes (a) through (c) show the seasonal curves generated for all pixels corresponding to the noted criterion. The Area Under Curve (AUC) difference indicates the total difference in temperature over the course of a year, while the peak difference indicates the maximum vertical difference between the two curves. Note that all y axis units are °C, and all x axes represent 1 year.

(degree-weeks), given that the STA curves are drawn as a function of weeks of the year. The calendar summer months were used to isolate the period during which the UTC/LST relationship was potentially strongest, based on deciduous leaf area. To represent divergences from persistence across the entire range of net UTC change, the AUC of the beginning-of-series curve was subtracted from that of the end-of-series to yield the annual change in degree-weeks. In order to account for the 2008 UTC starting condition, the AUC differencing process was run for four 2008 fractional UTC bins: 0% to 25%, 25% to 50%, 50% to 75%, 75% to 100%, and 0% to 100% (i.e. all pixels). These bins differentiate landcover composition prior to any UTC change, such that pixels that started with 75% coverage and loss 50% could be analyzed separately from those that started with 25% and lost 50%.

5. Results

5.1. UTC mapping

The combination of fine spatial resolution imagery with Lidar-derived canopy metrics produced a high-quality UTC map, providing appropriate units of analysis for the subsequent LST change analysis. The baseline, pixel-based RF classification produced a Kappa Index of Agreement (KIA) of 0.65, corresponding to an overall accuracy of 82.8% and an overall error of 17.4%. Modulation of the four segmentation parameters produced maps of both higher and lower accuracy than a baseline pixel-based classification (Figs. 3 and 4). The peaks on these figures indicate the optimal segmentation parameters, found to be: window 3, similarity tolerance 5, mean weight 0.3 and variance weight 0.7.

Classified maps produced using the optimal parameters yielded a KIA of 0.72, corresponding to an overall error rate and accuracy of 14.2% and 85.8%, respectively. The final UTC map is shown in Fig. 5, panel (a), whose extent is centered on the Burncoat and Greendale neighborhoods of Worcester. An overlay of UTC change analysis is shown in Fig. 5, panel (b). The area of UTC persistence (net UTC change > -5% and < 5%) was 4890 ha, while UTC loss (net UTC change < 5%) 3863 ha, and gain (net UTC change > 5%) was 1064 ha. Loss occurred in woodlots due to new development, and the residential areas of Burncoat and Greendale and other neighborhoods due to ALB-caused tree removal, as shown previously by Hostetler et al. (2013). UTC gain occurred in from new tree plantings in residential locations, as well as along existing forest edges.

5.2. LST time series analysis

The three LST/UTC regressions for 2008, 2010, and 2015 were significant at a 0.01 confidence level, and all produced similar results, as indicated by Table 2. The explained variance for all regressions was between 40 and 42%, with roughly a 5.5 °C decrease caused by a 100% UTC increase.

The baseline for temperature deviations was taken to be the temperature change in UTC persistence locations. Any temperature trend in persistence locations can be assumed to be part of a larger temporal and/or spatial scale weather or climate trend, not mediated by UTC. This background trend is provided by the monotonic Theil-Sen (TS) median trend analysis. Monotonic trends for all UTC bins are shown in Fig. 6, which indicates a decreasing trend of TS median slopes with increasing net UTC change, as expected. Aggregated persistence locations for the entire study area show a TS median slope of 0.014789 °C/year, implying a slight temperature increase. Both UTC gain and loss locations showed higher TS median slopes as high as 0.023201 °C/year for 95% UTC loss and 0.01015 °C/year for 95% UTC gain. While all locations showed positive TS median slopes, the persistence locations showed the smallest slope, while gain and loss showed intermediate and highest slopes, as could be expected based on UTC-caused cooling.

Table 2
Regression outputs from the three time periods of UTC and the associated LST pixels.

	Intercept	Slope	R	R2
2008	301.111	−5.7	−0.6333	0.4012
2010	303.575	−5.54	−0.65	0.4221
2015	303.6	−5.63	−0.65	0.4216
Mean of parameters	302.762	−5.62333	−0.64443	0.414967

STA results for the entire study area are shown in Fig. 7, which shows the seasonal temperature curves for all persistence (net UTC change >−5% and <5%) (a), all losses (net UTC change <−5%) (b), and all gains (net UTC change >5%) (c) locations, respectively. These curves represent the aggregated LST cycle for the first and last two years of the study period, and show distinct temperature trends for UTC loss locations versus gain and persistence. Each pane's corresponding AUC difference and peak difference metrics indicate the difference between beginning- and end-of-series seasonal curves. The baseline for comparison, persistence, shows a peak difference of 2 °C between the beginning and end of the time series, with an increase of 74 degree-weeks, calculated from the difference between beginning and ending AUC. All loss pixels show a slightly larger peak difference of 2.4 °C, while gain areas show the smallest peak difference of 1.6°. AUC differences are commensurate, with loss showing the largest (89.1 degree-weeks) and gain showing the smallest (64.6 degree-weeks). However, because STA curves were created for each 10%-wide net UTC bin, more detail concerning the LST/UTC relationship is available, as illustrated by Fig. 8.

Fig. 8 shows the AUC differences during the summer period when the potential UTC/LST relationship is strongest, and shows different lines representing the range of initial UTC coverage in 2008. The values on the graph are relative to the persistence value of each 2008 UTC coverage bin, as a baseline. The majority of UTC loss bins for all 2008 coverage proportions show an AUC difference greater than persistence, except the −35% to −25% bin for the 50% to 75% and all pixels starting conditions, which show values just less than 0. This indicates a larger increase in temperatures for loss pixels than for persistence. The greatest LST increases were associated with the greatest loss of UTC, with the 25–50% starting condition indicating the overall highest change. All gain bins show AUC differences less than or equal to persistence, implying a smaller difference over the time period for areas with new UTC. Gain bins showed smaller absolute differences from persistence than loss bins, with a less clear trend overall. However, as each bin approached its maximum potential coverage, seasonal LST increases were minimized, as shown most clearly by the 50–75% line.

Table 3 summarizes these STA curves in a different way, showing various warm-up and cool-down thresholds, where each row indicates a percent of the maximum LST value, and the date columns indicate the date associated with that value as it increases (warm-up) and decreases (cool-down). The table also shows the total number of days of seasonal elongation, and the number of days of elongation minus the persistence elongation, for reference. All three UTC conditions were measured in this way, using ±5% as the persistence criterion, and corresponding negative or positive proportions for loss and gain, respectively. The table indicates that for any given warm-up/cool-down threshold, net UTC loss areas experienced longer periods of elevated temperatures than persistence or gain areas, relative to each treatment's respective 2007 seasonality.

Zooming into the neighborhoods with largest UTC loss (Fig. 9), a broad-area LST trend is apparent. The square query box shown in

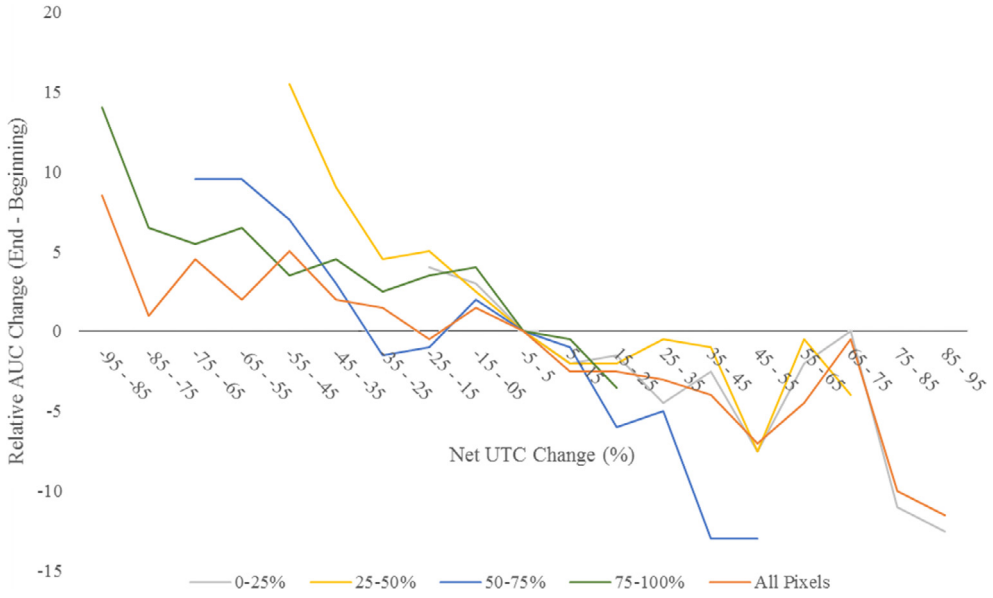

Fig. 8. Area Under Curve (AUC) differences between the beginning and end Seasonal Trend Analysis (STA) curves for various Urban Tree Canopy (UTC) change thresholds. The different lines indicate different 2008 UTC cover proportions, with orange indicating any starting condition (i.e. all pixels). This figure indicates that as net UTC loss increases, the difference between STA curves from beginning to end of series also increases, indicating seasonal Land Surface Temperature (LST) increases.

Table 3
Seasonal timing of Land Surface Temperature (LST) as derived by Seasonal Trend Analysis (STA), showing warm-up and cool-down dates for various thresholds, for loss, gain, and persistence locations, respectively. Each threshold represents the percentage of maximum LST achieved. The warm up/down difference columns indicate the difference in attainment of the given threshold from the beginning to the end of the series, reported in decimalized days. The seasonal elongation columns represent the difference between the absolute values of the preceding two columns, with the right-most column indicating the seasonal elongation of gain or loss minus that of persistence, the baseline.

UTC Persistence (Net UTC <5% and >−5%)								
	Series Beginning (2007)		*Series End (2015)*					
Percent of annual maximum temperature	Warm-up	Cool-down	Warm-up	Cool-down	Warm-up difference (days)	Cool-down difference (days)	Seasonal elongation	Seasonal elongation relative to persistence
25	23-Feb	21-Nov	19-Feb	1-Dec	−3.65	10.2	13.85	0
50	19-Mar	26-Oct	18-Mar	3-Nov	−1.26	7.88	9.14	0
75	14-Apr	26-Sep	13-Apr	5-Oct	−1.15	8.22	9.37	0
100	5-Feb	9-Dec	25-Jan	27-Dec	−10.9	17.5	28.4	0
UTC Gain (Net UTC > 5%)								
	Series Beginning (2007)		*Series End (2015)*					
Percent of Annual Maximum Temperature	Warm-Up	Cool-down	Warm-Up	Cool-down	Warm-Up Difference (Days)	Cool-down Difference (Days)	Seasonal Elongation	
25	22-Feb	22-Nov	15-Feb	30-Nov	−6.62	8.21	14.83	0.98
50	18-Mar	27-Oct	14-Mar	1-Nov	−3.57	5.67	9.24	0.1
75	12-Apr	27-Sep	9-Apr	3-Oct	−2.7	6.38	9.08	-0.29
100	4-Feb	10-Dec	20-Jan	27-Dec	−15.6	17	32.6	4.2
UTC Loss (Net UTC < −5%)								
	Series Beginning (2007)		*Series End (2015)*					
Percent of annual maximum temperature	Warm-up	Cool-down	Warm-up	Cool-down	warm-up difference (days)	Cool-down difference (days)	Seasonal elongation	
25	22-Feb	21-Nov	17-Feb	4-Dec	−4.87	13.5	18.37	4.52
50	18-Mar	26-Oct	16-Mar	5-Nov	−2.5	10.3	12.8	3.66
75	13-Apr	27-Sep	10-Apr	7-Oct	−3.49	10.3	13.79	4.42
100	4-Feb	9-Dec	19-Jan	4-Jan	−16.5	26	42.5	14.1

Fig. 9 indicates an area with mean net UTC change of −23%; the STA curves generated from this location show a 4 °C higher peak LST (July) for the end of the series relative to the beginning, as well as a longer summer temperature duration of 11.58 days, as indicated by the sum of the 75% warm-up/cool-down thresholds specific to this location. Elevated temperatures can also be observed between loss and persistence locations at the end of the time series. Gain locations showed intermediate temperature increases relative to persistence and loss, with a 3 °C increase in summer peak temperature. A warmer-than-average winter in 2013 caused elevated seasonal curves for the end of series curves (in red), as determined by the *in situ* weather station data; therefore, the winter deviations in seasonal curves are not due to UTC changes.

Additional results of neighborhood-scale analysis are shown in Fig. 10, which shows an areas of UTC persistence directly adjacent to these neighborhoods. Whereas previous graphs were generated for the entire study area with UTC net change bins, these two figures show the seasonal graphs as calculated for a square sample region indicated on the map. This technique highlights subsets of the study area of particular interest, rather than indicating the aggregated effects of UTC loss or persistence.

Parcel-scale analyses of UTC loss focused on the LST changes caused by the removal of individual or small groups of trees (as illustrated by Fig. 11). This figure shows the change in LST seasonal curves for the highlighted tree loss polygon, which in this case represents a single large tree. This particular tree removal, typifying

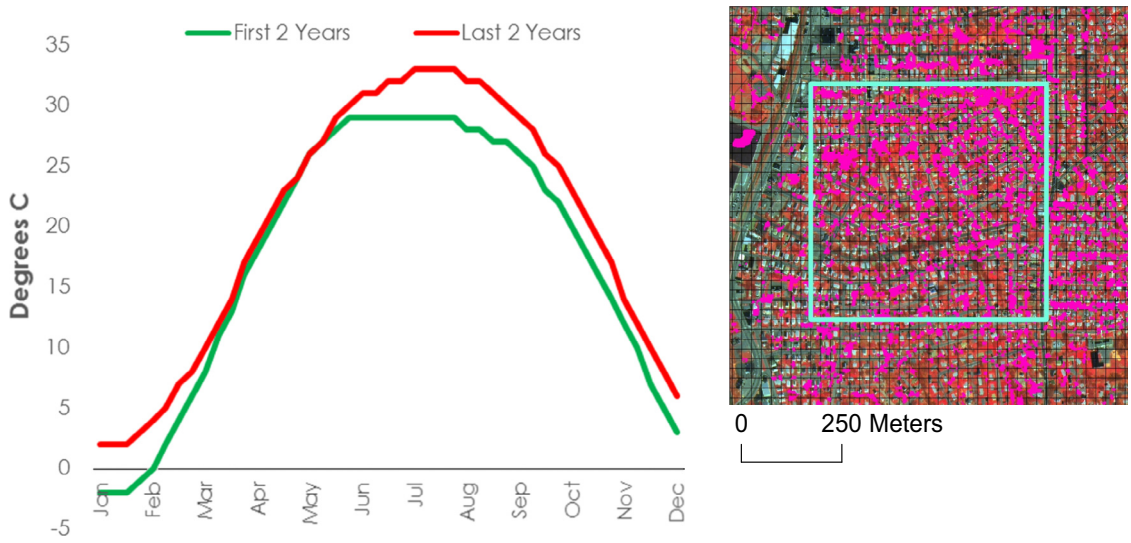

Fig. 9. STA for large portion of the Burncoat and Greendale neighborhoods in north Worcester, MA, as indicated by the square subsample, highlighted in cyan. These areas were hardest-hit by the ALB-related tree removal effort, and therefore saw considerable UTC reduction between 2008 and 2010. The area within the cyan square showed a net UTC change of −23.0% between 2008 and 2010, with limited regrowth by 2015, showing a net UTC change of 0.5%.

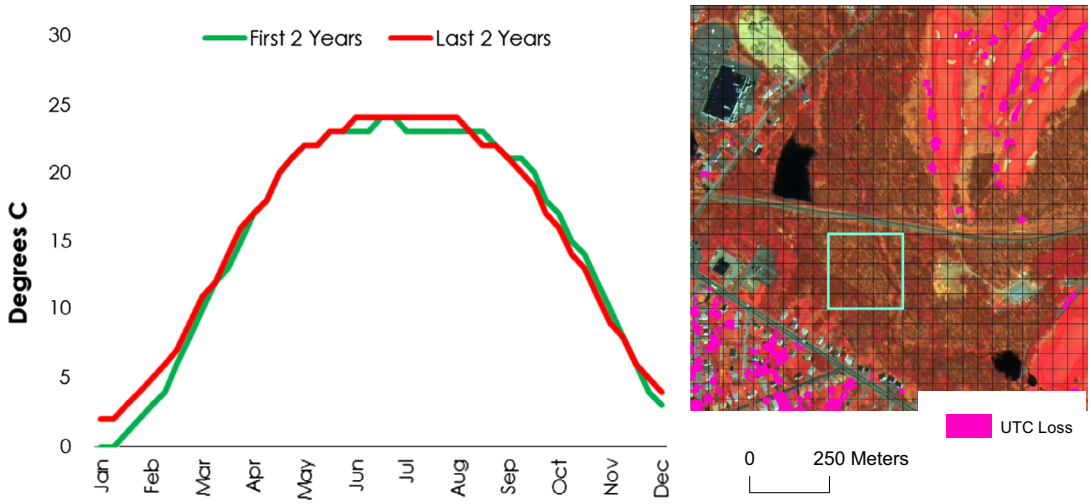

Fig. 10. STA graph and corresponding map for a persistent woodland area adjacent to the Burncoat and Greendale neighborhoods. This area showed less than 1% net UTC change between 2008 and 2015.

many similar locations, is associated with a marked increase in both summer temperature and length, with peak season increase of 4 °C, representing a 15% increase from the pre-loss condition. Additionally, this location experiences an increase of summer duration of approximately 3 days.

Street-scale analysis of UTC loss revealed larger increases in LST compared to the parcel-scale. Granville Avenue, shown in Fig. 12, typifies the areas with maximum UTC decrease. This street experienced a nearly complete removal of all UTC, which had previously comprised mature *Acer* spp. shade trees. This loss is shown by the highlighted polygons in the figure. Consequently, peak LST increased by 5 °C during July and August, a 19% increase from pre-loss conditions, and the summer season was prolonged by 8 days.

Seasonal timing of LST was also altered by UTC loss, as indicated by Table 3. The right-most columns indicate the change in warm-up and cool-down dates in days, with negative values indicating an earlier date of percentage attainment from the beginning to the end of the series, and positive values indicating a later date of percentage attainment from the beginning to the end of the series. This table quantifies the pattern of earlier warm-up and delayed cool-down evident in Figs. 9 and 11, particularly indicating that cool-down tended to occur later in the year the loss class, relative to the persistence class.

6. Discussion

6.1. UTC mapping

Traditional field methods and manual image interpretation of UTC can provide highly detailed inventories and cover estimates, but do not produce detailed or wall-to-wall information on tree cover locations (Freeman and Buck, 2003; Moskal et al., 2011; O'Neil-Dunne et al., 2014; Pu and Landry, 2012). This paper illustrates the effectiveness of fine spatial resolution remote sensing products for UTC mapping and inventory applications, particularly using image segmentation methods combined with freely available

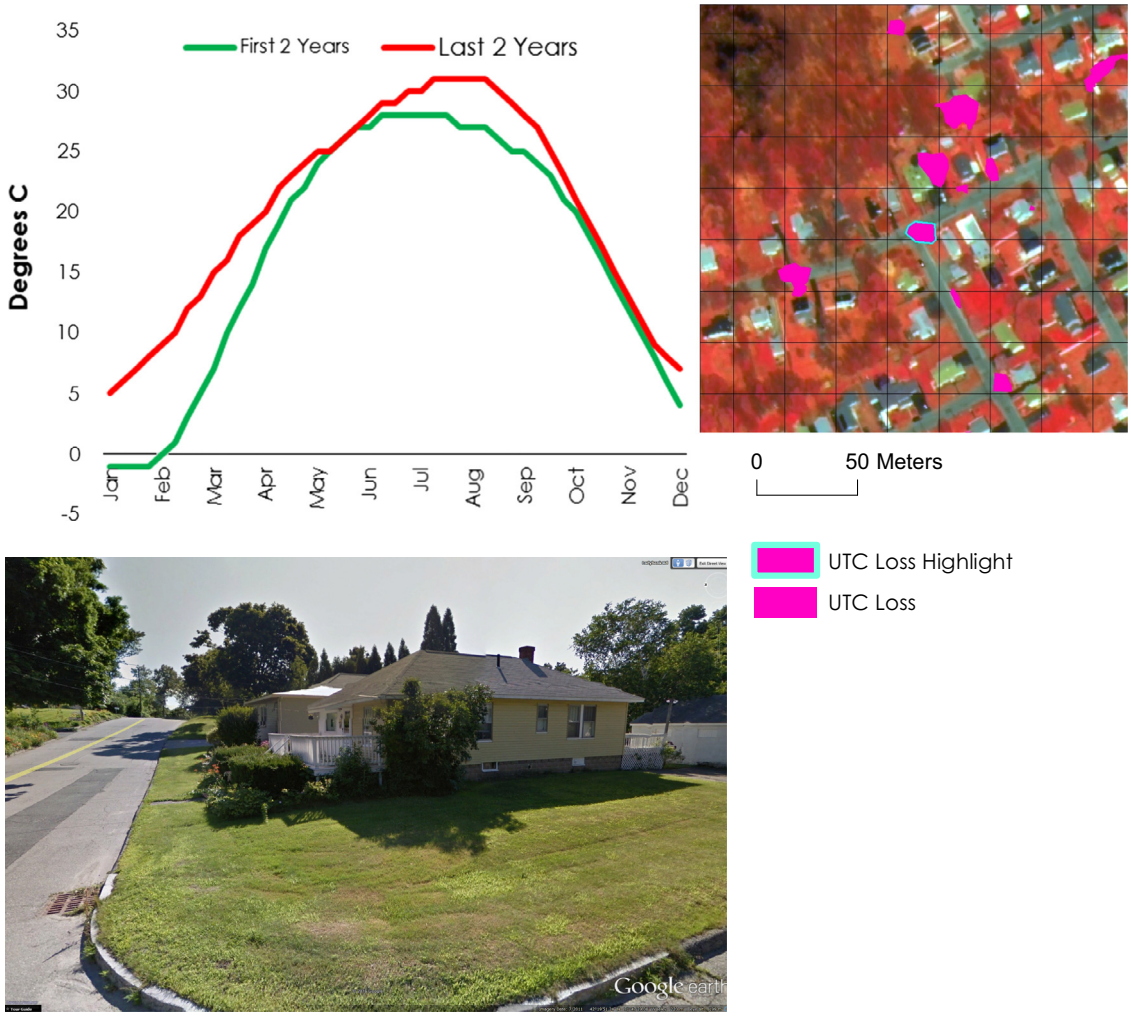

Fig. 11. The STA graph can be created for a single pixel, such as in this case of a typical single tree removal, as shown in satellite imagery (top left) and in Google Street View™. The pixel containing the highlighted tree showed a net UTC decrease of 16.9% between 2008 and 2010, corresponding with the loss of the tree.

Lidar and fine spatial resolution imagery. Although WorldView-2 data are not free, NAIP aerial imagery may be used as a free substitute. Lidar, also freely available for certain areas, provides valuable canopy structural information, which facilitates precise tree/non-tree segmentation that is particularly helpful for discriminating trees from other green vegetation. The spectral and spatial detail contributed by the WorldView-2 imagery allows for separation of tree segments from other, typically man-made, objects with vertical structure, such as buildings, telephone poles, and streetlights.

Segmentation was conducted using two different input datasets: a combination of Lidar and spectral (i.e. all eight Lidar-derived rasters and also all eight WorldView-2 spectral bands), and using only the Lidar-derived rasters. Optimal results were found using the Lidar-only dataset, as the spectral bands tended cause under-segmentation of vegetation, combining adjacent tree and grass or shrub areas into single image segments. This under-segmentation is likely the result of similar vegetation spectral signature, shared by grass, shrubs, and trees. Rigorous accuracy comparison of lidar-only versus lidar-and-spectral bands was omitted from this paper for brevity, but for a small test site, typical KIA values for spectral and Lidar segmentation ranged between 0.2 and 0.4, while for Lidar-only segmentation, using the same pixel-based classification input, typical values ranged from 0.4 to 0.7.

Parameterization of segmentation algorithms is not straightforward, since the size, shape, and texture of target objects may be unique for a particular user and application (Blaschke, 2010; Mathieu et al., 2007; Pu and Landry, 2012). The TerrSet segmentation implementation requires just four parameters, but nevertheless the appropriate values for these parameters may be different for each mapping application, and even with only a small range of experimental values for each parameter, the number of combinations is potentially quite large. This implementation is particularly difficult given that remotely sensed imagery spans a wide range of Ground Sample Distances (GSD) and therefore pixel dimensions, implying that the user must consider the relationship between target objects and image spatial resolution. Therefore, this paper proposes a 'scale free' approach, in which segmentation parameters are not defined *a priori*, but rather are determined empirically based on previously-created validation points, using parameter iteration with modulation. This procedure is similar to that of previous studies that have relied on trial-and-error to determine optimal segmentation parameters (e.g., Mathieu et al., 2007), but because optimization is based on previously determined validation points, it can be viewed as an objective approach. The procedure finds the best combination of parameters regardless of the object-to-pixel size ratio or any other object properties, and is therefore applicable to a wide range of imagery and target object types. Furthermore, this type of procedure is software agnostic, provided the user's selected software can be accessed via a scripting or command-line interface. The segmentation algorithm in TerrSet is rather straightforward compared to that of a dedicated object-based software such as eCognition (and the license fee is

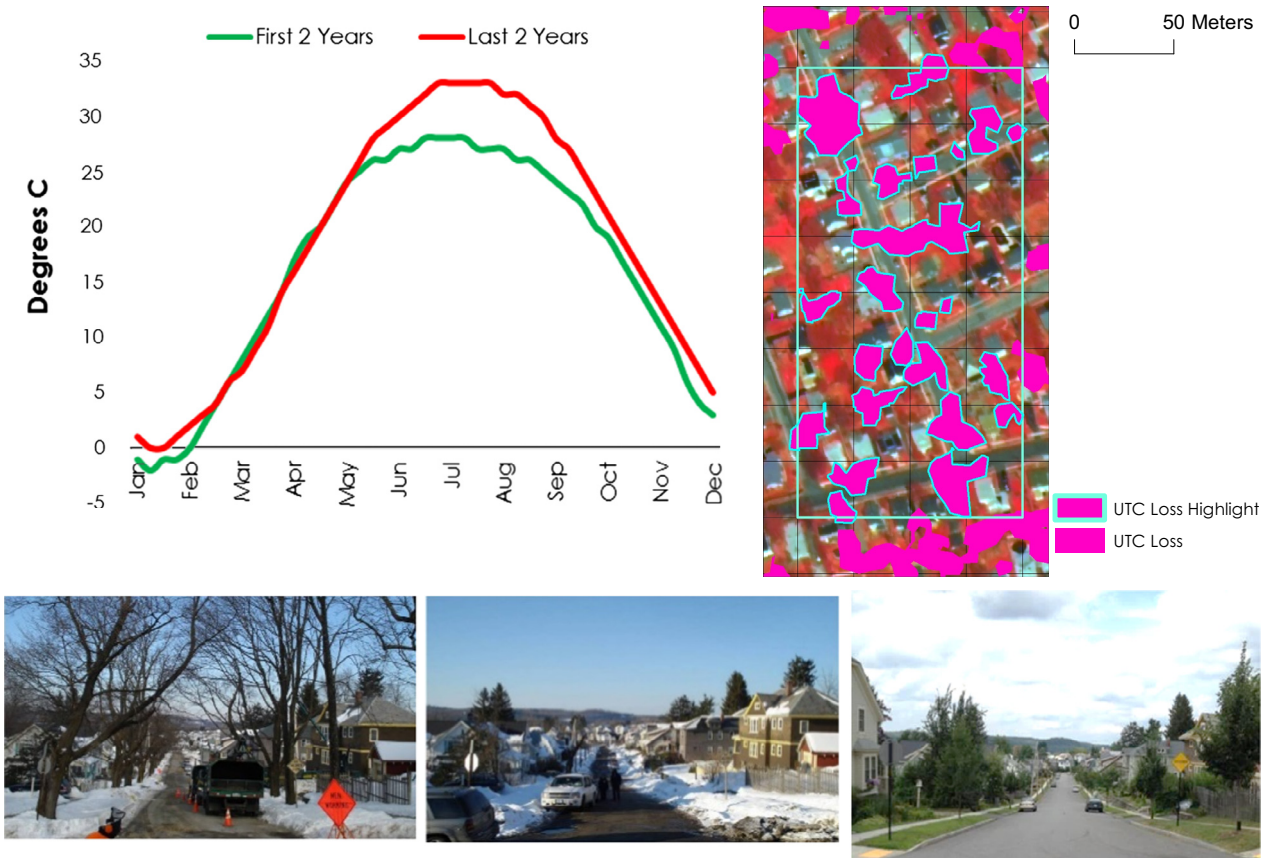

Fig. 12. STA for Granville Avenue in the Greendale neighborhood. The street-level photos show the UTC change from 2008 to 2015, while the highlighted polygons on the map show mapped UTC loss and the black grid shows the Landsat-scale units of analysis. The STA graph indicates an increase of 6 °C during August. The location indicated by the square sample region saw a −23.2% net UTC change from 2008 to 2015.

considerably lower), and the procedures outlined by this paper produced high quality, segmentation-based UTC maps. The segmentation parameters ultimately used in this analysis may also be well suited for different datasets of similar resolution, but it is likely that different input data would yield different optimal parameters, and thus the parameter selection process should be run for each new study area.

Change analysis typically relies on data from the same sensor or suite of sensors, which removes problems associated with change of GSD, spectral resolution, and radiometric calibration. However, because fine spatial resolution sensors cover small swaths and require large revisit times (or considerable expense and different viewing angles), it is often necessary to complete change mapping with multiple sensors and/or platforms. This analysis required fine spatial resolution (~1 m) UTC maps for three time periods, and therefore drew on maps produced using both aerial imagery and a combination of satellite and aerial Lidar data. The 2008 and 2010 UTC maps had a reported positional accuracy of ±2 m, meaning that some misclassification of UTC was possible. Additionally, since the 2015 UTC map drew on slightly different datasets, it is possible that some error was produced between the 2008, 2010, and 2015 maps. Although these UTC maps have slightly different spatial characteristics, as shown in Fig. 5, the feature detection was overall deemed to be high quality, and acceptable UTC change detection.

6.2. LST time series analysis

UTC provides several valuable ecosystem services, and is increasingly seen to be an indispensable component of sustainable city design (Nowak and Greenfield, 2012; Nowak and Dwyer, 2007). Of particular note is the mitigation of the urban heat island effect by urban trees, caused by increased evaporative cooling and canopy shade provision (McPherson and Simpson, 2003). It is essential to understand the magnitude of this ecosystem service, and Worcester provides an excellent test scenario for this goal, because it has experienced a large degree of canopy loss and regrowth during a relatively short time.

The spatial relationship between LST and UTC was demonstrated by the OLS regressions for each year of available UTC data, and is reflected in Table 2. The coefficient of determination (R^2) of these relationships was around 0.40–0.42. This shows a moderate amount of explanatory power from UTC fractional coverage, but given the range of variables potentially affecting LST at any given pixel, these numbers were considered reasonably large. Within a single time period, UTC coverage fraction was shown to be responsible for a roughly 5.5 °C difference in LST, which is commensurate in magnitude to the STA findings discussed below.

The monotonic trend results provide a temporal metric that shows the effect of UTC change on LST. Theil-Sen median slope values were highest for UTC loss bins and lowest for gain bins, implying that presence of trees slowed the increase of temperatures during the study time period, relative to locations of UTC persistence. UTC persistence locations provide a suitable basis for comparison to gain and loss, as they capture the background trend in LST over the time period, and it can be assumed that any trend in areas of no UTC change is caused by external climate or weather variability. The slight monotonic increase in LST for persistence locations was outpaced by all loss bins, while gain bins tended to show lower monotonic increases, suggesting that UTC change is

indeed driving these LST increases. The slightly stronger effect of UTC loss than UTC gain on LST change can be explained by the fact that UTC in this case is a two-dimensional measure of cover, and does not incorporate tree vertical structure or canopy volume, and therefore cannot incorporate the total leaf area or height of the trees. Since much of the UTC loss reflected the removal of mature shade trees and UTC gains include small, juvenile trees, the LST mitigation of UTC gain is smaller than loss.

Seasonal Trend Analysis results confirm the results of the monotonic trend analysis, showing that, irrespective of 2008 UTC fractional coverage (i.e. the starting condition), the majority of net UTC loss bins showed a larger AUC difference than persistence, indicating warmer summer periods for locations with high amounts of tree loss (Fig. 8). Locations with less initial coverage showed a larger increase in LST magnitude than areas with greater initial coverage for an equal amount of UTC loss, highlighting the importance of even partial tree coverage. Furthermore, all gain bins indicated a smaller or equal AUC difference than for persistence area, meaning that any amount of UTC gain equated to a cooling benefit, or at worst no change. While the gain bins showed a weaker, less clear signal of LST seasonality than the loss bins, the change to maximum tree coverage was always associated with an increase in LST mitigation, and all change bins outside the 55–75% range showed LST mitigation. This suggests that small, newly planted trees may have a measurable impact on LST seasonality, although an extended time series will be necessary to confirm and nuance this relationship, and to determine the anomalous 55–75% bins.

The extension of the warm season in UTC loss areas is further quantified by the proportional warm-up/down information provided by Table 3. This table indicates seasonal extensions ranging from 3.66 to 14.1 days for UTC loss areas, relative to persistence. This corroborates the AUC difference metrics, and provides the additional information of days of extended season, a metric potentially more useful or interesting to policy makers or members of the interested public. UTC gain areas also show slight seasonal extensions relative to persistence, except for using the 75% warm-up/down threshold. However, the divergence from persistence is quite small, ranging from 0.1 to 4.2 days. Furthermore, the 100% threshold, the largest divergence for both gain and loss, indicates the difference in peak temperature attainment, and may not be as useful for season-long comparisons.

Taking individual, parcel-scale observations in increasingly large aggregations shows the street-, neighborhood-, and city-scale UTC loss effects, as shown in Figs. 7–12. Fig. 9, showing seasonal curves for the whole neighborhood of Burncoat/Greendale irrespective of the UTC change polygons, shows that the large quantity of UTC loss in the worst-impacted neighborhoods have driven aggregate LST increases that overwhelm the cooling provided by smaller magnitude UTC gains and persistent trees. This figure also shows that the entire neighborhood experienced an elongated period of elevated temperatures. Therefore, although clear heterogeneity of LST seasonality exists within the study area, contingent on individual tree/stand removal, the overall trend at the largest scale of analysis is of increasing LST due to the large decrease in UTC cover. UTC gain locations show somewhat mitigated LST increases caused by newly planted juvenile trees, but the UTC loss effect is much stronger since it indicates the loss of large, mature shade trees.

LST increases of the magnitude shown could potentially cause significant increases in home cooling costs, especially when viewed in aggregate of an entire urban area. It should be emphasized that much of the UTC loss in Worcester occurred on private residences, often exposing grass and other vegetation rather than impervious surface, as may be expected in a more heavily urbanized area with 'street trees'. Because vegetated surfaces inherently experience less heat retention and thus SUHI, it should be expected that tree loss in more densely urbanized areas will exhibit an even stronger effect on LST.

Future work will extend the time series of analysis to further track the growth of newly planted trees, and quantify the ongoing LST reductions caused by new UTC coverage. Quantification of LST reductions by trees at various growth stages will facilitate predictions of future ecosystem services by the urban forest. This future work will rely on extended Landsat LST time series, relying primarily on Landsat-8, and also on high-resolution UTC maps created using the methods outlined in this paper. Incorporation of field data for tree and stand dimensions may help refine future UTC maps.

7. Conclusions

This paper contributes substantive empirical knowledge on the relationship between UTC loss and LST seasonal dynamics, lending further support to the notion that UTC significantly reduces LST, even in low-density, residential neighborhoods with existing vegetation. Such areas are less susceptible to the SUHI because of their more natural material composition, and so the cooling effect of UTC is likely to create a smaller signal. Nevertheless, this signal was isolated in this research at city, neighborhood, street, and parcel scales. This research highlights the importance of urban forests for the vital ecosystem service provision of reduced SUHI, and illustrates the effectiveness of remote sensing for monitoring urban forests and LST.

Overall, this research demonstrates the capacity for data fusion and thermal image analysis to effectively monitor urban forest inventories. This research also illustrates an important application of UTC change detection by exploring the relationship between UTC and LST at a fine scale and using a combination of methods that have not been used by any previous study. LST was shown to increase with decreasing UTC, and canopy regeneration was also shown to be associated with reduced LST, although this relationship was weaker given the limited amount of time provided for tree growth. Furthermore, STA revealed that summer LST increased in both magnitude and duration for UTC loss areas, exacerbating SUHI effects and potentially causing increases in home cooling costs. Using a multi-scale approach allows for measurement of changes to temperature magnitude and timing from parcel- to neighborhood-scales, which provides invaluable information to individual residents, land managers, and city policy makers.

Acknowledgements

The authors would like to thank the DigitalGlobe corporation for the generous provision of imagery, without which this project would not have been possible. We would also like to thank Mat Cahill of the Massachusetts Department of Conservation and Recreation for his valuable insights and contributions. Finally, we thank the Worcester Tree Initiative for their guidance and support.

References

Akbari, H., 2002. Shade trees reduce building energy use and CO_2 emissions from power plants. Environ. Pollut. 116, S119–S126.

Berk, A., Anderson, G.P., Acharya, P.K., Hoke, M.L., Chetwynd, J.H., Bernstein, L.S., 2003. MODTRAN4 Version 3 Revision 1 User's Manual. Geophysics Laboratory, Hanscom Air Force Base, MA.

Blaschke, T., 2010. Object based image analysis for remote sensing. ISPRS J. Photogramm. Remote Sens. 65, 2–16. http://dx.doi.org/10.1016/j.isprsjprs.2009.06.004.

Breiman, L., 2001. Random forests. Mach. Learn. 45, 1–35. http://dx.doi.org/10.1023/A:1010933404324.

Brenner, J.C., Christman, Z., Rogan, J., 2012. Segmentation of Landsat Thematic Mapper imagery improves buffelgrass (Pennisetum ciliare) pasture mapping in

the Sonoran Desert of Mexico. Appl. Geogr. 34, 569–575. http://dx.doi.org/10.1016/j.apgeog.2012.02.008.
Cristóbal, J., Jiménez-Muñoz, J.C., Sobrino, J.A., Ninyerola, M., Pons, X., Cristóbal, J., Jiménez-Muñoz, J.C., Sobrino, J.A., Ninyerola, M., Pons, X., 2009. Improvements in land surface temperature retrieval from the Landsat series thermal band using water vapor and air temperature. J. Geophys. Res. Atmos. 114, 1–16. http://dx.doi.org/10.1029/2008JD010616.
Cui, Y.Y., De Foy, B., 2012. Seasonal variations of the urban heat island at the surface and the near-surface and reductions due to urban vegetation in Mexico City. J. Appl. Meteorol. Climatol. 51, 855–868.
Dalponte, M., Bruzzone, L., Gianelle, D., 2008. Fusion of hyperspectral and LIDAR remote sensing data for classification of complex forest areas. IEEE Trans. Geosci. Remote Sens. 46, 1416–1427. http://dx.doi.org/10.1109/TGRS.2008.916480.
Dash, P., Göttsche, F.-M., Olesen, F.-S., Fischer, H., 2002. Land surface temperature and emissivity estimation from passive sensor data: theory and practice-current trends. Int. J. Remote Sens. 23, 2563–2594. http://dx.doi.org/10.1080/01431160110115041.
Dey, V., Zhang, Y., Zhong, M., 2010. A review on image segmentation techniques with remote sensing perspective. na.
DigitalGlobe, 2015. WorldView-2 panchromatic scenes, Level Standard 2A. Longmont, Color.
Dodds, K.J., Orwig, D.A., 2011. An invasive urban forest pest invades natural environments—Asian longhorned beetle in northeastern US hardwood forests. Can. J. For. Res. 41, 1729–1742.
Eastman, J.R., 2015. TerrSet Geospatial Monitoring and Modeling Software.
Eastman, J.R., Sangermano, F., Ghimire, B., Zhu, H., Chen, H., Neeti, N., Cai, Y., Machado, E.A., Crema, S.C., 2009. Seasonal trend analysis of image time series. Int. J. Remote Sens. 30, 2721–2726. http://dx.doi.org/10.1080/01431160902755338.
Freeman, C., Buck, O., 2003. The development of a land use decision making model for use on sites with naturally regenerating habitat. Development of an ecological mapping methodology for urban areas in New Zealand. Landsc. Urban Plan. 63, 161–173.
Freilicher, M., 2011. Tree by tree, yard by yard: replanting Worcester's trees. Arnoldia 69, 1–13.
Freilicher, M., Kane, B.C., Ryan, H.D.P., 2008. A Report on the Status of Street Trees in Worcester, Massachusetts Trees in Peril : Responding to the Asian Longhorned Beetle.
Hall, B., Motzkin, G., Foster, D.R., Syfert, M., Burk, J., 2002. Three hundred years of forest and land-use change in Massachusetts, USA. J. Biogeogr. 29, 1319–1335.
Hamada, S., Ohta, T., 2010. Seasonal variations in the cooling effect of urban green areas on surrounding urban areas. Urban For. Urban Green. 9, 15–24. http://dx.doi.org/10.1016/j.ufug.2009.10.002.
Herwitz, E., 2001. Trees at Risk: Reclaiming an Urban Forest, a Case History of Worcester. Chandler House Press, Massachusetts.
Hostetler, A.E., Rogan, J., Martin, D., DeLauer, V., O'Neil-Dunne, J., 2013. Characterizing tree canopy loss using multi-source GIS data in Central Massachusetts, USA. Remote Sens. Lett. 4, 1137–1146. http://dx.doi.org/10.1080/2150704X.2013.852704.
Huth, R., Pokorná, L., 2004. Parametric versus non-parametric estimates of climatic trends. Theor. Appl. Climatol. 77, 107–112. http://dx.doi.org/10.1007/s00704-003-0026-3.
Jiménez-Muñoz, J.C., Cristóbal, J., Sobrino, J.A., Sòria, G., Ninyerola, M., Pons, X., 2009. Revision of the single-channel algorithm for land surface temperature retrieval from Landsat thermal-infrared data. Geosci. Remote Sensing, IEEE Trans. 47, 339–349.
Jiménez-Muñoz, J.C., Sobrino, J.A., 2003. A generalized single-channel method for retrieving land surface temperature from remote sensing data. J. Geophys. Res. Atmos., 108
Jiménez-Muñoz, J.C., Sobrino, J.A., Skokovic, D., Mattar, C., Cristóbal, J., 2014. Land surface temperature retrieval methods from landsat-8 thermal infrared sensor data. Geosci. Remote Sens. Lett. IEEE 11, 1840–1843. http://dx.doi.org/10.1109/LGRS.2014.2312032.
Ke, Y., Quackenbush, L., 2007. Forest species classification and tree crown delineation using quickbird imagery. In: ASPRS 2007 Annu. Conf. 9.
Kim, S.-R., Lee, W.-K., Kwak, D.-A., Biging, G.S., Gong, P., Lee, J.-H., Cho, H.-K., 2011. Forest cover classification by optimal segmentation of high resolution satellite imagery. Sensors 11, 1943–1958. http://dx.doi.org/10.3390/s110201943.
Li, Z.-L., Becker, F., 1993. Feasibility of land surface temperature and emissivity determination from AVHRR data. Rem. Sens. Environ. 43, 67–85.
Li, Z.-L., Tang, B.-H., Wu, H., Ren, H., Yan, G., Wan, Z., Trigo, I.F., Sobrino, J.a., 2013. Satellite-derived land surface temperature: current status and perspectives. Remote Sens. Environ. 131, 14–37. http://dx.doi.org/10.1016/j.rse.2012.12.008.
Maimaitiyiming, M., Ghulam, A., Tiyip, T., Pla, F., Latorre-Carmona, P., Halik, Ü., Sawut, M., Caetano, M., 2014. Effects of green space spatial pattern on land surface temperature: implications for sustainable urban planning and climate change adaptation. ISPRS J. Photogramm. Remote Sens. 89, 59–66. http://dx.doi.org/10.1016/j.isprsjprs.2013.12.010.
Mathieu, R., Aryal, J., Chong, A.k., 2007. Object-based classification of ikonos imagery for mapping large-scale vegetation communities in urban areas. Sensors 7, 2860–2880. http://dx.doi.org/10.3390/s7112860.
McPherson, E.G., Nowak, D.J., Rowntree, R.A., 1994. Chicago's Urban Forest Ecosystem: Results of the Chicago Urban Forest Climate Project.
McPherson, E.G., Simpson, J.R., 2003. McPherson and Simpson Potential energy savings in buildings by an urban tree planting programme in California.pdf. Urban For. Urban Green. 2, 73–86.
Mitraka, Z., Chrysoulakis, N., Kamarianakis, Y., Partsinevelos, P., Tsouchlaraki, A., 2012. Improving the estimation of urban surface emissivity based on sub-pixel classification of high resolution satellite imagery. Remote Sens. Environ. 117, 125–134. http://dx.doi.org/10.1016/j.rse.2011.06.025.
Morzuch, E., 2013. The Energy Benefits of Trees: Investigating Shading, Microclimate and Wind Shielding Effects in Worcester and Springfield, Massachusetts. Masters Theses 1911 - Febr. 2014.
Moskal, L.M., Styers, D.M., Halabisky, M., 2011. Monitoring urban tree cover using object-based image analysis and public domain remotely sensed data. Remote Sens. 3, 2243–2262. http://dx.doi.org/10.3390/rs3102243.
Neeti, N., Rogan, J., Christman, Z., Eastman, J.R., Millones, M., Schneider, L., Nickl, E., Schmook, B., Turner, B.L., Ghimire, B., 2011. Mapping seasonal trends in vegetation using AVHRR-NDVI time series in the Yucatán Peninsula, Mexico. Remote Sens. Lett. 3, 433–442. http://dx.doi.org/10.1080/01431161.2011.616238.
Nowak, D., Greenfield, E., 2012. Tree and impervious cover change in US cities. Urban For. Urban Green. 11, 21–30.
Nowak, Dwyer, 2007. Understanding the benefits and costs of urban forest ecosystems. In: Urban and Community Forestry in the Northeast. Springer, pp. 25–46.
O'Neil-Dunne, J., MacFaden, S., Royar, A., 2014. A versatile, production-oriented approach to high-resolution tree-canopy mapping in urban and suburban landscapes using GEOBIA and data fusion. Remote Sens. 6, 12837–12865. http://dx.doi.org/10.3390/rs61212837.
Oke, T.R., 1982. The energetic basis of the urban heat island. Q. J. R. Meteorol. Soc. 108, 1–24.
Ottle, C., Stoll, M., 1993. Effect of atmospheric absorption and surface emissivity on the determination of land surface temperature from infrared satellite data. Int. J. Remote Sens. 14, 2025–2037.
Palmer, S., Martin, D., DeLauer, V., Rogan, J., 2014. Vulnerability and adaptive capacity in response to the Asian longhorned beetle infestation in Worcester, Massachusetts. Hum. Ecol. 42, 965–977. http://dx.doi.org/10.1007/s10745-014-9695-z.
Pandit, R., Laband, D.N., 2010. Energy savings from tree shade. Ecol. Econ. 69, 1324–1329.
Pu, R., Landry, S., 2012. A comparative analysis of high spatial resolution IKONOS and WorldView-2 imagery for mapping urban tree species. Remote Sens. Environ. 124, 516–533. http://dx.doi.org/10.1016/j.rse.2012.06.011.
R Core Team, 2013. R: A Language and Environment for Statistical Computing.
Rogan, J., Bumbarger, N., Kulakowski, D., Christman, Z.J., Runfola, D.M., Blanchard, S. D., 2010. Improving forest type discrimination with mixed lifeform classes using fuzzy classification thresholds informed by field observations. Can. J. Remote Sens. 36, 699–708. http://dx.doi.org/10.5589/m11-009.
Rogan, J., Ziemer, M., Martin, D., Ratick, S., Cuba, N., DeLauer, V., 2013. The impact of tree cover loss on land surface temperature: a case study of central Massachusetts using Landsat Thematic Mapper thermal data. Appl. Geogr. 45, 49–57.
Santos, R., Cole, L., 2012. Massachusetts Asian Longhorned Beetle Cooperative Eradication Program Determines Next Steps for Eradication Efforts in Worcester County.
Schmidt, G., Jenkerson, C., Masek, J., Vermote, E., Gao, F., 2013. Landsat ecosystem disturbance adaptive processing system (LEDAPS) algorithm description. Open-File Rep.
Sobrino, J.A., Jiménez-Muñoz, J.C., Paolini, L., 2004. Land surface temperature retrieval from LANDSAT TM 5. Remote Sens. Environ. 90, 434–440. http://dx.doi.org/10.1016/j.rse.2004.02.003.
Sobrino, J.A., Jiménez-Muñoz, Juan C., Sòria, Guillem, Romaguera, M., Guanter, L., Moreno, J., Plaza, A., Martínez, P., 2008. Land surface emissivity retrieval from different VNIR and TIR sensors. IEEE Trans. Geosci. Remote Sens. 46, 316–327. http://dx.doi.org/10.1109/TGRS.2007.904834.
Sobrino, J.A., Raissouni, N., 2000. Toward remote sensing methods for land cover dynamic monitoring: application to Morocco. Int. J. Remote Sens. 21, 353–366. http://dx.doi.org/10.1080/014311600210876.
Solecki, W.D.W., Rosenzweig, C., Parshall, L., Pope, G., Clark, M., Cox, J., Wiencke, M., 2005. Mitigation of the heat island effect in urban New Jersey. Environ. Hazards 6, 39–49.
Strahler, A., Woodcock, C., Smith, J., 1986. On the nature of models in remote sensing. Remote Sens. Environ. 20, 121–139.
Valor, E., Caselles, V., 1996. Mapping land surface emissivity from NDVI: Application to European, African, and South American areas. Remote Sens. Environ. 57, 167–184. http://dx.doi.org/10.1016/0034-4257(96)00039-9.
Van de Griend, A., Owe, M., 1993. On the relationship between thermal emissivity and the normalized difference vegetation index for natural surfaces. Int. J. Remote Sens. 14, 1119–1131.
Voogt, J.A., Oke, T.R., 2003. Thermal remote sensing of urban climates. Remote Sens. Environ. 86, 370–384. http://dx.doi.org/10.1016/S0034-4257(03)00079-8.
Wan, Z., Dozier, J., 1996. A generalized split-window algorithm for retrieving land-surface temperature from space. IEEE Trans. Geosci. Remote Sens. 34, 892–905. http://dx.doi.org/10.1109/36.508406.
Weng, Q., 2009. Thermal infrared remote sensing for urban climate and environmental studies: methods, applications, and trends. ISPRS J. Photogramm. Remote Sens. 64, 335–344. http://dx.doi.org/10.1016/j.isprsjprs.2009.03.007.

Weng, Q., 2001. A remote sensing – GIS evaluation of urban expansion and its impact on surface temperature in the Zhujiang Delta, China. Int. J. Remote Sens. 22, 1999–2014. http://dx.doi.org/10.1080/713860788.

Weng, Q., Liu, H., Lu, D., 2007. Assessing the effects of land use and land cover patterns on thermal conditions using landscape metrics in city of Indianapolis, United States. Urban Ecosyst. 10, 203–219. http://dx.doi.org/10.1007/s11252-007-0020-0.

WTI, 2015. Worcester Tree Initiative Homepage [WWW Document]. <http://www.treeworcester.org/>.

Zhu, Z., Woodcock, C.E., 2012. Object-based cloud and cloud shadow detection in Landsat imagery. Remote Sens. Environ. 118, 83–94. http://dx.doi.org/10.1016/j.rse.2011.10.028.